Wear xxx (xxxx) 205961

Contents lists available at ScienceDirect

Wear

journal homepage: www.elsevier.com/locate/wear

Additively manufactured and cast high-temperature aluminum alloys for electric vehicle brake rotor application

Tomas Grejtak [a,*], Amit Shyam [a], Peter J. Blau [b], Jun Qu [a,**]

[a] Materials Science and Technology Division, Oak Ridge National Laboratory, Oak Ridge, TN, 37831, USA
[b] Blau Tribology Consulting, Enka, NC, 28715, USA

ARTICLE INFO

Keywords:
Brake rotor
Aluminum alloys
Additive manufacturing
Electric vehicles
Transfer layer

ABSTRACT

Electric vehicle brake rotors demand lightweight, high thermal conductivity materials with good resistance to wear, creep, salt corrosion, and thermal fade, all of which present challenges to the traditionally used cast iron. In this work, we investigated the braking performance of recently developed high-temperature aluminum alloys in both cast and 3D printed forms, that possess excellent microstructural and mechanical stability at elevated temperatures. Three aluminum alloys, Al-6Cu-Mn-Zr, Al-9Cu-Mn-Zr, and Al-Ce-Ni-Mn-Zr and a reference cast iron were tested on a sub-scale brake tester against a commercial brake pad material over a range of sliding speeds between 2 and 15 m/s. The performance of these alloys was evaluated for wear resistance, friction behavior, temperature elevation, and surface morphological change. Although all three candidate alloys had lower wear-resistance than cast iron, Al-Ce-Ni-Mn-Zr showed a significantly reduced wear rate in comparison to the Al-Cu-Mn-Zr alloys. Moreover, Al-Ce-Ni-Mn-Zr alloy had the most consistent friction behavior at all sliding speeds and good fade resistance, as the coefficient of friction did not dramatically decrease with temperature rise but stayed within a desirable range of 0.35–0.50 instead. The superior wear resistance and braking performance of the Al-Ce-Ni-Mn-Zr alloy were attributed to its higher hardness, and high temperature yield strength and creep resistance compared with the Al-Cu-Mn-Zr alloys. The results suggest that the braking performance of these aluminum alloys could be further enhanced by increasing the hardness and forming a more stable transfer layer on the sliding surface.

1. Introduction

Structural materials used in the braking system play a critical role in ensuring safety for ground-based transportation systems. In rotor brake systems, braking relies on the friction generated between the rotor and the pad to slow down or stop the vehicle [1,2]. This process can eventually lead to undesired wear of the brake rotor, pad, and other components [2–6]. Besides offering acceptable wear-resistance, brake system materials must possess corrosion resistance [6,7], good thermal conductivity to reduce surface temperature due to frictional heating [8–10], and fade resistance to resist a decrease in friction at elevated temperatures [11–13]. Gray cast iron is the most commonly used material for brake rotors in passenger vehicles and heavy trucks due to its favorable properties such as wear-resistance, preservation of structural integrity and mechanical properties at elevated temperatures, and relatively low cost [2,6]. On the other hand, gray cast iron is higher in density, has low thermal conductivity, and is prone to corrosion, all of which are undesirable features for brake systems [14].

In recent years, the demand for electric vehicles (EVs) has rapidly increased mainly due to a global effort to reduce carbon emissions [15]. EVs are fundamentally different from internal combustion engine (ICE) vehicles. That has led to design several modifications of EVs. One of the most distinct differences between ICE vehicles and EVs is the braking system. In EVs, most of the braking is facilitated by the electric motor slowing down the vehicle by converting kinetic energy into electrical energy, which is stored in the battery, in a process called regenerative braking [15] [16]. Less frequent use of conventional braking presents an opportunity to replace traditionally used cast iron brake rotors with lighter alternatives. Candidate replacement materials need to possess a combination of properties to enable reliable braking. Although regenerative braking reduces demand on the wear performance of the brake rotors, the alternative materials need to be tribologically compatible with the brake pad material to minimize wear and to meet the typical coeffi-

This article is part of a special issue entitled: WOM2025 published in Wear.

* Corresponding author. Materials Science and Technology Division, Oak Ridge National Laboratory, Oak Ridge, TN, 37831, USA.
** Corresponding author.
E-mail addresses: grejtakt@ornl.gov (T. Grejtak), qujn@ornl.gov (J. Qu).

https://doi.org/10.1016/j.wear.2025.205961
Received 23 September 2024; Received in revised form 16 January 2025; Accepted 6 February 2025
0043-1648/© 20XX

cient of friction (COF) requirement of 0.35–0.5 [1]. Curiously, one particular challenge arises when the brakes are not being used for a long period of time, such as during long-distance driving or when the vehicle is not being used for several days. During these times, moisture naturally builds up on brake rotors and pads. In ICE vehicles, the brakes are used often, so the moisture evaporates before it can cause corrosion. In contrast, EVs use regenerative braking to slow down the vehicle and thus the brakes are used less frequently, which allows rust to build up and potentially deteriorate both rotors and pads [7] [14] [17] [18]. Therefore, brake rotors materials used in EVs need adequate corrosion resistance. Additionally, frictional heating generated during braking requires preservation of strength, fatigue, and creep resistance at elevated temperatures. Rotors experience thermo-mechanical fatigue due to repeated braking, which results in the generation of surface cracks [4] [19]. Lastly, weight increases power consumption which essentially reduces the driving range. According to the National Research Council, a 10 % mass reduction can improve the fuel efficiency of a passenger vehicle by 6–7% [20]. Moreover, EVs are heavier than their ICE counterparts because of the around 1000 pounds of batteries. Cast iron rotors are considerably heavy and reducing weight of the EV components is a particular strategy to increase their range.

One of the alternative materials to potentially replace the traditionally used cast iron are Al alloys. Al alloys are lighter (~3 vs ~ 7 g/cm^3), more corrosion resistant, and more thermally conductive than cast iron. A comprehensive study by Awe et al., compared the brake performance of Al-SiC composite rotors to gray cast iron rotors using a dynamometer and a vehicle test [17]. The results showed that the Al-SiC rotor had no wear and formed a stable transfer film which is essential for lowering the wear and friction. Additionally, the Al-SiC rotor had significantly lower particle emission, lower surface temperature, and much higher corrosion than the reference cast iron rotor. In a separate study by Lyu et al., a pin-on-disk tribological characterization of an AlSiC metal-matrix-composite (MMC) disk on a non-asbestos organic brake pad pair showed that the disk did not exhibit any wear due to formation of a transfer film [21]. In another pin-on-disc study by Du et al., it was demonstrated that Al-SiC MMC forms a transfer film when sliding against a commercial pad material which allowed improvement in the wear-resistance [22]. Modeling efforts supported by experiments in the work by Zang et al., showed that SiC particles in SiCp/Al composite rotors cause microcracks which is induced by repeated thermo-mechanical loading [4]. Application of plasma electrolytic oxidation (PEO) surface treatment on Al alloy and metal composite brake rotors has also been evaluated in the work by Gulden et al. [23]. It was demonstrated that PEO surface treatment increases the hardness of Al alloy and metal composites and maintains a satisfactory friction performance. Other light-weight material systems were studied as well. In the past, Oak Ridge National Laboratory (ORNL) evaluated the feasibility of applying titanium alloys as brake rotor materials [13,24,25]. Comprehensive brake testing characterization showed that although the braking performance of Ti alloys did not outperform cast iron, the wear-resistance was significantly improved by applying thermal sprayed coating. However, a disadvantage of Ti alloys is their low thermal conductivity which results in very high surface temperatures. It should be noted that the performance of rotor materials greatly depends on the compatibility with the pad material. Brake pads could be metallic, semi-metallic, ceramic or organic and usually contain different friction modifiers, binders and fillers. Composition of a commercial pad material is typically proprietary which makes developing and designing brake rotor materials more challenging.

Nevertheless, the braking performance of Al alloy and composite rotors could be enhanced by improving their high temperature resistance. In recent years, a series of high temperature aluminum alloys has been developed which demonstrated exceptional microstructural and mechanical stability beyond 300 °C [26–33] which makes them promising candidates for rotor materials in EVs. These alloys are cast Al-Cu-Mn-Zr [27,30–32] and additively manufactured (AM) Al-Ce-Ni-Mn-Zr [26,28,33]. Al-Cu alloys are commonly used in automotive engines due to their strength, good castability, and relatively low cost [34–36]. Strengthening mechanism in Al-Cu alloys is facilitated by metastable θ′ (Al_2Cu) precipitates [37], however, temperatures above 250 °C lead to transformation and coarsening of the metastable precipitates, which results in the softening of the alloy. In cast Al-Cu-Mn-Zr alloys, the addition of Mn and Zr has been shown to stabilize the microstructure and improve the coarsening resistance at temperatures up to 350 °C, which consequently increased the hardness and strength [27,30,31]. Challenges of AM Al-alloys are coarsening of strengthening phases and grain structure refinement which cause a low creep resistance [38]. Emerging eutectic systems such as Al-Ce have good printability and they also exhibit high temperature coarsening resistance of their strengthening phases [33,39,40]. In Al-Ce-Ni-Mn-Zr alloys, the improved mechanical properties due to formation of strengthened microstructures have been linked to the rapid solidification enabled by AM [26] [28] [33].

This work investigates the potential of advanced high temperature Al-6Cu-Mn-Zr, Al-9Cu-Mn-Zr, and Al-Ce-Ni-Mn-Zr alloys as brake rotor materials. Evaluation was based on drag-type sliding friction and wear data from a custom-made sub-scale brake tester using a commercial brake pad material designed for Al alloy rotors. In addition to wear and friction measurements, frictional heating and microstructural analyses were performed on the rotor and pad sliding surfaces.

2. Materials and methods

2.1. Rotor materials

Cast aluminum alloys were fabricated in the form of multiple chill plate castings at Wolverine Bronze, MI. Two copper concentrations (6 wt% and 9 wt%) were studied in the cast alloys to make two Al-Cu-Mn-Zr alloys whose compositions are shown in Table 1. The dimensions of the cast plates were approximately 50.8 × 152 × 229 mm. Rotors with a diameter of 125.4 mm and thickness of 6.35 mm were machined from the plates with a final surface finish of < 0.1 μm. The rotors were solution treated at 540 °C for 5 h, quenched in 80 °C water, and then aged at 240 °C for 5 h prior to brake testing.

Additively manufactured (AM) Al-Ce-Ni-Mn-Zr rotors, Fig. 1a, were fabricated using laser powder bed fusion (LPBF) with sieved powder in the size range of 20–63 μm (Beehive Industries) with an EOS M290 machine, using 370 W power, 1300 mm/s scanning speed, 0.19 mm hatch spacing, and 30 μm layer thickness. Oversized rotors were printed on a 170 °C preheated build plate under an Ar atmosphere, with the axis of rotors oriented along the build direction. The AM rotor specimens were subsequently machined and finished to the same dimensions and a similar surface finish as the cast rotors.

All brake rotors were polished with a fly cutter on a HAAS milling machine using a custom-made adjustable steel cutter with a carbide insert. The final roughness of the polished rotors is shown in Table 2.

Table 1
Composition of rotor materials in %wt.

Rotor material	Cu	Si	Zn	Fe	Ni	Mn	Zr	Ti	Ce	Al
Al-6Cu-Mn-Zr	6.23	0.068	0.063	0.077	–	0.471	0.157	0.084	–	bal.
Al-9Cu-Mn-Zr	8.86	0.095	0.077	0.057	–	0.426	0.161	0.068	–	bal.
Al-Ce-Ni-Mn-Zr		0.075	–	0.11	4.5	0.40	0.76		8.3	bal.

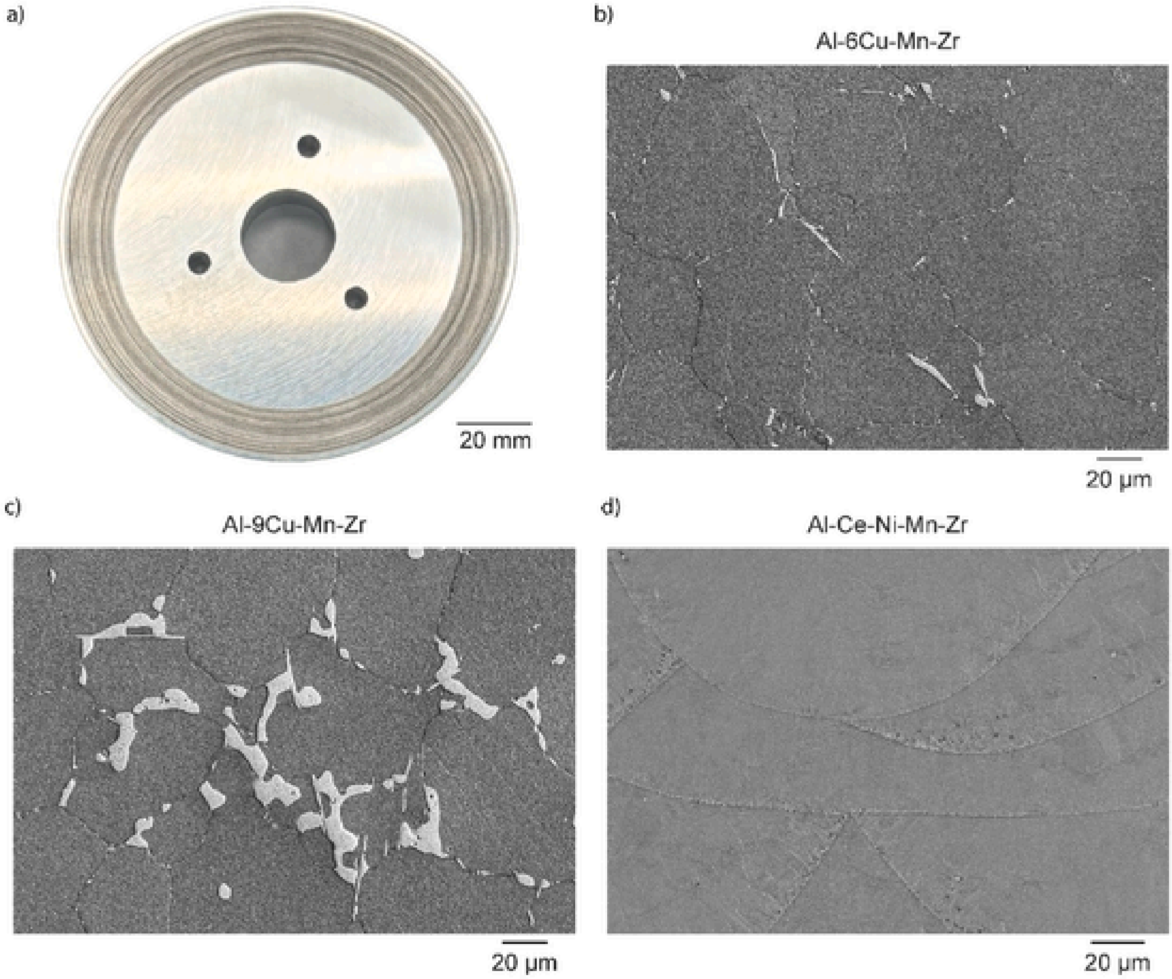

Fig. 1. a) Image of the AM rotor fabricated from the candidate Al-Ce-Ni-Mn-Zr alloy. SEM images of a) heat-treated cast Al-6Cu-Mn-Zr, b) heat-treated cast Al-9Cu-Mn-Zr, and c) as-printed AM Al-Ce-Ni-Mn-Zr.

Table 2
Properties of the brake rotor materials used in this study.

Rotor material	Vickers hardness (HV0.1)	Density (g/cm^3)	Roughness (R_a) (μm)
Al-6Cu-Mn-Zr	105.8 ± 8.1	2.9	0.08 ± 0.02
Al-9Cu-Mn-Zr	120.9 ± 8.7	2.8	0.09 ± 0.01
Al-Ce-Ni-Mn-Zr	171.1 ± 7.6	2.9	0.17 ± 0.06
Cast iron	340.8 ± 28.7	7.1	0.17 ± 0.01

The SEM images revealing the microstructures of the Al-Ce-Ni-Mn-Zr, Al-6Cu-Mn-Zr and Al-9Cu-Mn-Zr rotors are shown in Fig. 1b,c,d, respectively. The dominant grain boundary phases (white) in Al-Cu-Mn-Zr alloys are Al_2Cu with some Al_7Cu_2Fe, Fig. 1b and c. Al-Ce-Ni-Mn-Zr consists mainly of $Al_{27}Ni6Ce_3$ with minor amounts of $Al_{11}Ce_3$ phases. More information about the grain structures and phases of these alloys can be found in Refs. [32,33].

2.2. Brake pad materials

Typically, brake pad materials are designed and formulated for wear and friction compatibility with a specific brake rotor material. The proprietary composition of commercial pad materials makes it very challenging to find a suitable match for candidate rotor materials. Efforts were made to find a compatible brake pad for the Al alloy rotors in this study. Over 15 commercial brake pad materials with varying compounds, including ceramic, metallic and graphite composites from different vendors were acquired and tested to look for compatibility between the brake pad and rotor materials. Based on the wear performance testing of the brake pads and the Al alloy rotors, Wilwood Purple Compound Brake Pad 150–13335K (Wilwood Engineering, Camarillo, CA, USA) was selected for this study. According to the manufacturer, this composite metallic compound brake pad was designed for Al rotors and is also compatible with iron and steel rotors. Squared block specimens with a 12.7 × 12.7 mm contact surface were cut from the brake pad using a bandsaw, Fig. 2a. The contact surface was polished with silicon carbide paper in the sequence of 240, 400 and 800 grits to a final arithmetic average surface roughness R_a of ~0.2 μm. The brake pad samples were then sonicated with isopropanol for 15 min prior to testing. Optical imaging, Fig. 2b and scanning electron microscopy (SEM) coupled with energy dispersive spectroscopy (EDS) elemental mapping, Fig. 2c and d, were conducted on the sliding surface of the pad to determine its composition, however, the exact compounds and formulation are unknown.

2.3. Vickers hardness

The hardness of the rotor materials was determined with a Vickers microindenter (Buehler, Model 1600–6305) at a 100 g-f load (HV0.1) on a polished surface. At least five measurements were taken to deter-

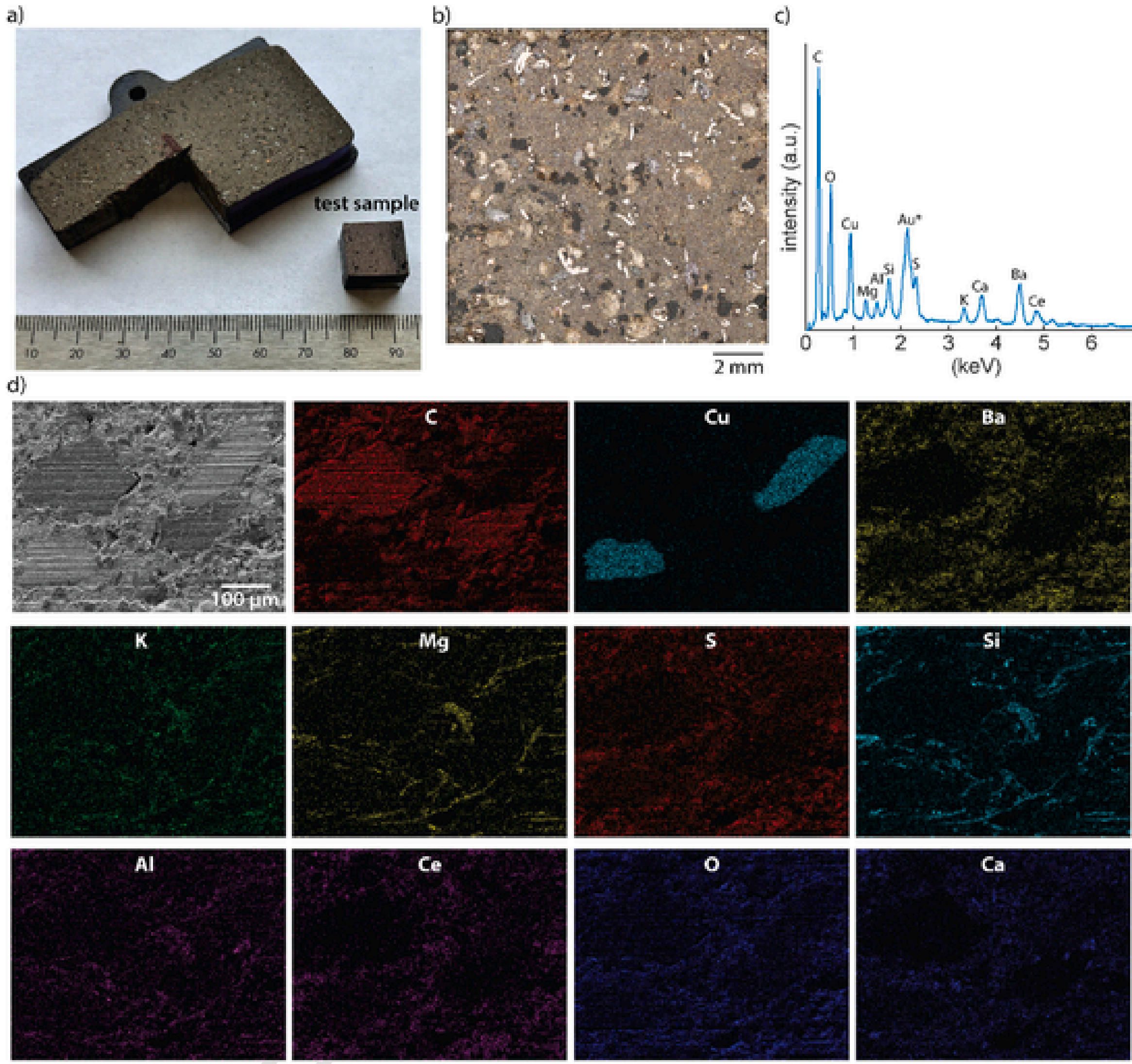

Fig. 2. Commercial brake pad material used in this work. a) Image of a sample cut from an actual brake pad, b) Optical microscopy image of a polished surface before testing, and c) EDS elemental spectra of the d) SEM image with corresponding EDS elemental mapping. *The sample was coated with Au to make the samples conductive for SEM imaging and EDS elemental mapping.

mine the mean and standard deviation hardness values shown in Table 2.

2.4. Surface roughness

The R_a was measured on a polished surface of the rotor material using a roughness tester with a contact stylus (Mahr Perthometer M2, Göttingen, Germany). The mean and standard deviation of the R_a values were calculated from three successive measurements taken at different locations of the rotor surface.

2.5. Thermophysical property measurements

The thermal conductivity of the Al-alloys was determined according to the ASTM standard E1461 using the laser flash technique. The specific heat capacity was measured using differential scanning calorimetry (Netzsch DSC 404C, Burlington, MA, USA) following the ASTM E1269. The measurements were taken at an interval of 50 °C from 450 °C to 50 °C for Al-Cu-Mn-Zr alloys and from 350 °C to 50 °C for Al-Ce-Ni-Mn-Zr alloy.

3. Brake testing procedure

3.1. Small-scale brake tester

Sliding friction and wear experiments were performed on the ORNL's sub-scale brake tester (SSBT) which had been used in the past to test brake performance of titanium-based brake rotors [13,24,25], Fig. 3. This equipment enables drag-type sliding contact between a brake pad and a rotor over a range of contact loads and sliding speeds. In this apparatus, the rotor is mounted to a 10 hp, 3-phase, variable-speed motor. A 12.7 × 12.7 mm square faced specimen cut from a brake pad is attached to a load head that consists of a pneumatic actuator to apply a normal load and a load cell to measure the tangential force. The SSBT is also equipped with an infrared (IR) sensor for in-situ measurements of the rotor temperature from the wear track during sliding. The temperature measurements using the IR sensor depend strongly on the material's emissivity. Prior to testing, the emissivity of all rotor materials was calibrated by heating the rotor on a hot plate to a temperature above 100 °C. During cooling, the temperature of the rotor's wear track was monitored with a surface thermocouple. Simultaneously, the IR temper-

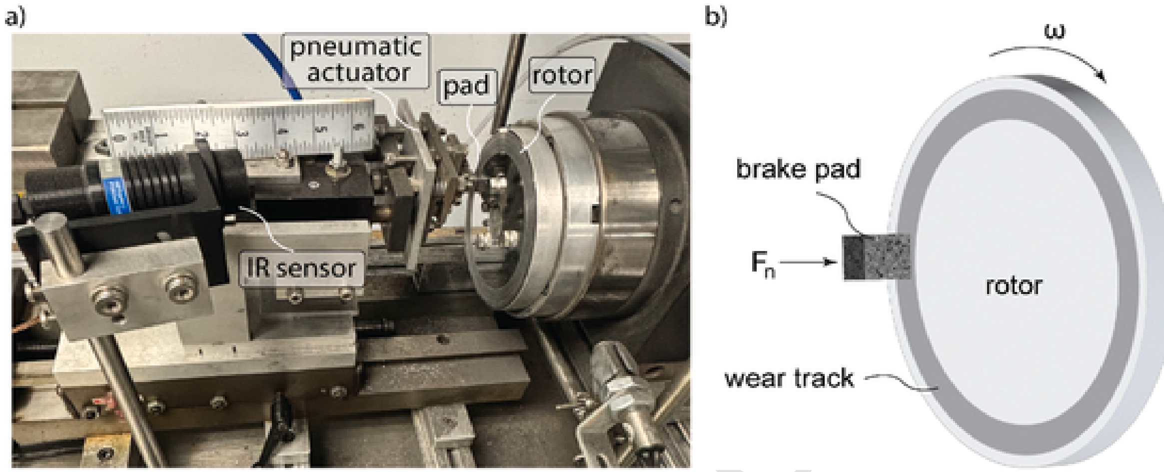

Fig. 3. SSBT apparatus. a) Image of the SSBT setup, b) Schematic of a sliding contact between the pad specimen and the rotor.

ature readings were taken from the wear track and the emissivity constant was adjusted to match the thermocouple temperature. The data acquisition was done with LabView™ software.

3.2. Brake testing protocol

The tests were performed at a constant load of 160N (equivalent of ~ 1 MPa contact pressure) and at four sliding speeds: 2, 6, 9.6, and 15 m/s which correspond to the vehicle's speeds of about 19, 57, 91.3, and 142.6 km/h, (11.9, 35.7, 57.1, and 89.2 mile/hr) respectively. Five repetitive drags were performed at each sliding speed, Fig. 4a. During each drag, the pad specimen was loaded against the rotating rotor for 20 s. The pad specimen was then unloaded momentarily for 10 s and then loaded again. After five consecutive drags, the rotor was allowed to cool for a duration of 1 min and the test procedure was repeated for a different sliding speed. The brake testing protocol is illustrated in Fig. 4b. The procedure consists of seven steps. Each step represents a specific sliding speed at which five drags were performed. The test protocol started with a sliding speed of 2 m/s, then increased to 6, 9.6, and 15 m/s, followed by decreasing 9.6, 6, and 2 m/s sliding speeds. The completion of this test procedure resulted in a total sliding distance of 5020 m (hereafter referred to as 5 km). A fresh (unworn) set of the brake rotor and pad was used at the beginning of the test protocol. The entire test procedure was then repeated using the same set of the rotor and pad with worn surfaces, yielding a total sliding distance of 10,040 m (hereafter referred to as 10 km). The wear performance of the rotor and the pad was evaluated after completion of each testing protocol while the COF and the rotor temperature were measured in-situ.

3.3. Wear quantification

The volumetric wear rate calculation procedure is illustrated in Fig. 5. After completion of the brake testing protocol, the wear track of the rotor materials, Fig. 5a, was scanned with a 3D white-light optical profiler (Veeco Wyko™ NT9100, USA) to determine the worn surface topography, Fig. 5b. The height data were then averaged to produce a mean worn surface profile (i.e., the mean cross-sectional area), Fig. 5c. The worn volume of the rotor was determined by multiplying the mean cross-sectional area by the perimeter of the circular wear track. The worn volume was then normalized by the applied load and the sliding distance. The wear performance of the rotors was also expressed as mass loss by multiplying the calculated worn volume by the rotor's density. The wear performance of the brake pad material was based on a direct measurement of the mass loss after each round of a brake testing protocol. The mass of the pad was measured at the beginning of the test and after completion of each of the two testing procedures using a scale (Sartorius Analytical BL-210S, Germany).

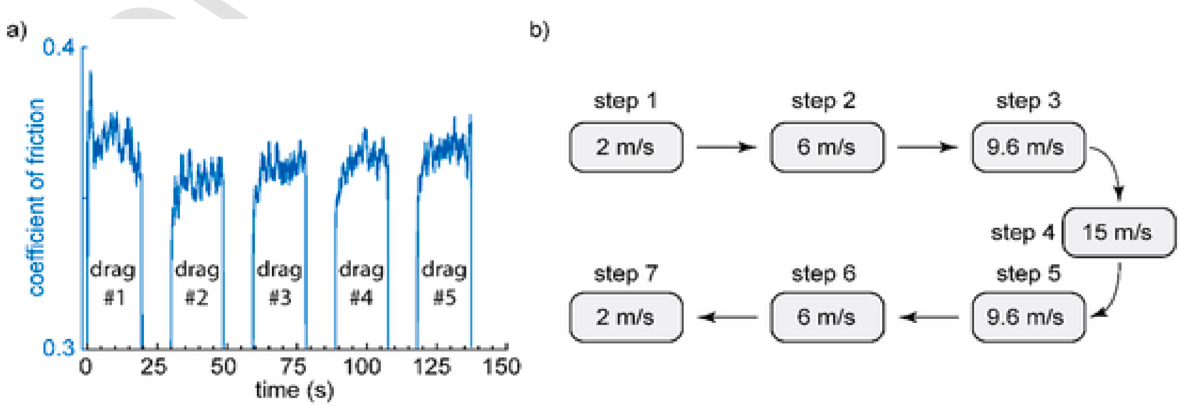

Fig. 4. Brake testing protocol. a) COF vs time of 5 consecutive drags performed at each sliding speed. b) Braking performance evaluation consisting of seven steps. Each step is composed of five consecutive drags.

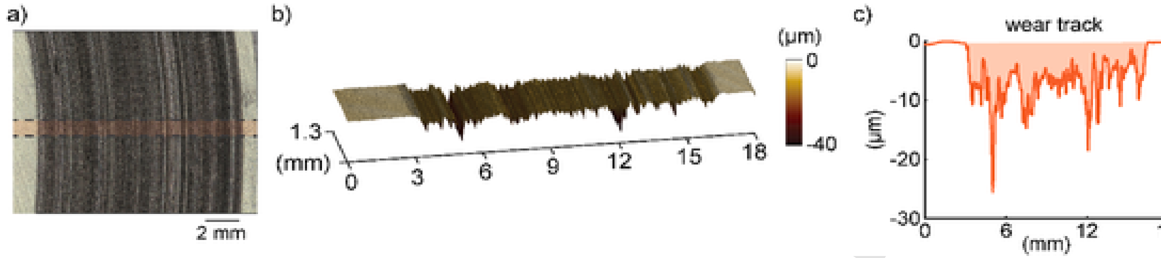

Fig. 5. Wear characterization for the rotor. a) Optical image of a wear track section depicting the measurement region in red, b) 3D worn surface topography, c) Average 2D worn surface profile determined from b). (For interpretation of the references to colour in this figure legend, the reader is referred to the Web version of this article.)

3.4. Microstructural characterization

The worn surface morphology and the elemental analysis of the rotor and the pad was conducted with SEM-EDS (Hitachi S4800, Japan and FEI Nova 200). The brake pad samples were coated with Au to make the sample surface electrically conductive to prevent charging effects. The worn surface morphology was also studied using an optical-3D laser confocal microscope (VKX-3000, Keyence, Osaka, Japan).

3.5. Frictional heating calculation

Frictional heating parameter Φ (W/m-K), which is a measure of the rotor track temperature change per unit of frictional work, was determined from in-situ measurements of the rotor temperature and COF as (13):

$$\Phi = \frac{\Delta T}{W} = \frac{\Delta T}{F_f x} = \frac{\Delta T}{\mu F_n x}, \quad (1)$$

where, ΔT (°C) is the average temperature change per drag and W (J) is the frictional work at a constant sliding speed. W can be expressed as the sliding distance x (m) times the frictional force F_f (N), where F_f is equal to the μ (COF) times the normal force F_n (N). Final value of Φ was then determined as an average Φ calculated at each sliding speed.

4. Results

4.1. Thermal conductivity

The thermal conductivity of the three Al alloys at 50–450°C is shown in Fig. 6. The thermal conductivities of the Al-6Cu-Mn-Zr and Al-9Cu-Mn-Zr alloys are very similar over the measured temperature range and are higher than that of the Al-Ce-Ni-Mn-Zr alloy. For all three alloys, the thermal conductivity increases with increasing temperature. The thermal conductivity of both Al-Cu-Mn-Zr alloys shows higher sensitivity to temperature which ranges from ~150 to ~200 W m^{-1} k^{-1}. On the other hand, the thermal conductivity of Al-Ce-Ni-Mn-Zr alloy is in a range of ~110–~125 W m^{-1} k^{-1} and is insensitive to the temperature change from 300 to 350 °C. The values at 100 °C of the measured thermal conductivity and specific heat are summarized in Table 3.

4.2. Frictional and temperature behavior

The analysis of the friction and temperature measurements was performed for the second round of 5 km sliding tests after the surface of the rotor and pad material were pre-worn. Fig. 7 depicts detailed results illustrating the in-situ measurements of both the COF and the rotor surface temperature throughout the entirety of the testing protocol of the Al-Ce-Ni-Mn-Zr rotor.

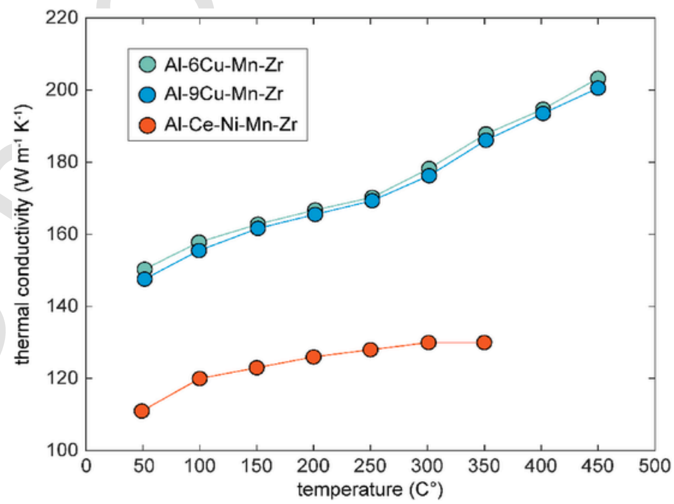

Fig. 6. Thermal conductivity of the Al-alloy rotors as a function of temperature.

Table 3
Summary of the thermal properties of the rotor materials based on the thermophysical property measurements and the brake testing results.

Rotor material	Thermal conductivity at 100 °C (W $m^{-1}k^{-1}$)	Specific heat capacity at 100 °C (J g^{-1} K^{-1})	Peak temp. (°C)	Avg. frictional heating (°C J^{-1})
Al-6Cu-Mn-Zr	158	0.90	144	1.0×10^{-3}
Al-9Cu-Mn-Zr	156	0.89	120	1.0×10^{-3}
Al-Ce-Ni-Mn-Zr	120	0.79	143	1.2×10^{-3}
Cast iron	32-52[41,42]	0.49–0.52[43]	212	1.5×10^{-3}

1 Step 1, speed 2 m/s: the COF reached ~0.4 in each of the five drags and the temperature slowly increased from the room temperature to ~35 °C.
2 Step 2, speed 6 m/s: the COF dropped to below 0.4 and remained constant for each of the five drags while the temperature increased more rapidly from 31 to 68 °C.
3 Step 3, speed 9 m/s: the COF remained consistently slightly below 0.4 and the temperature increased by 50 °C–104 °C. The temperature change per drag, ΔT [°C], is also significantly higher than that at 2 and 6 m/s sliding speeds.
4 Step 4, speed 15 m/s: the temperature increased from 77 °C to 143 °C which was the highest measured rotor temperature throughout the testing protocol. The ΔT was also the highest ~21°.

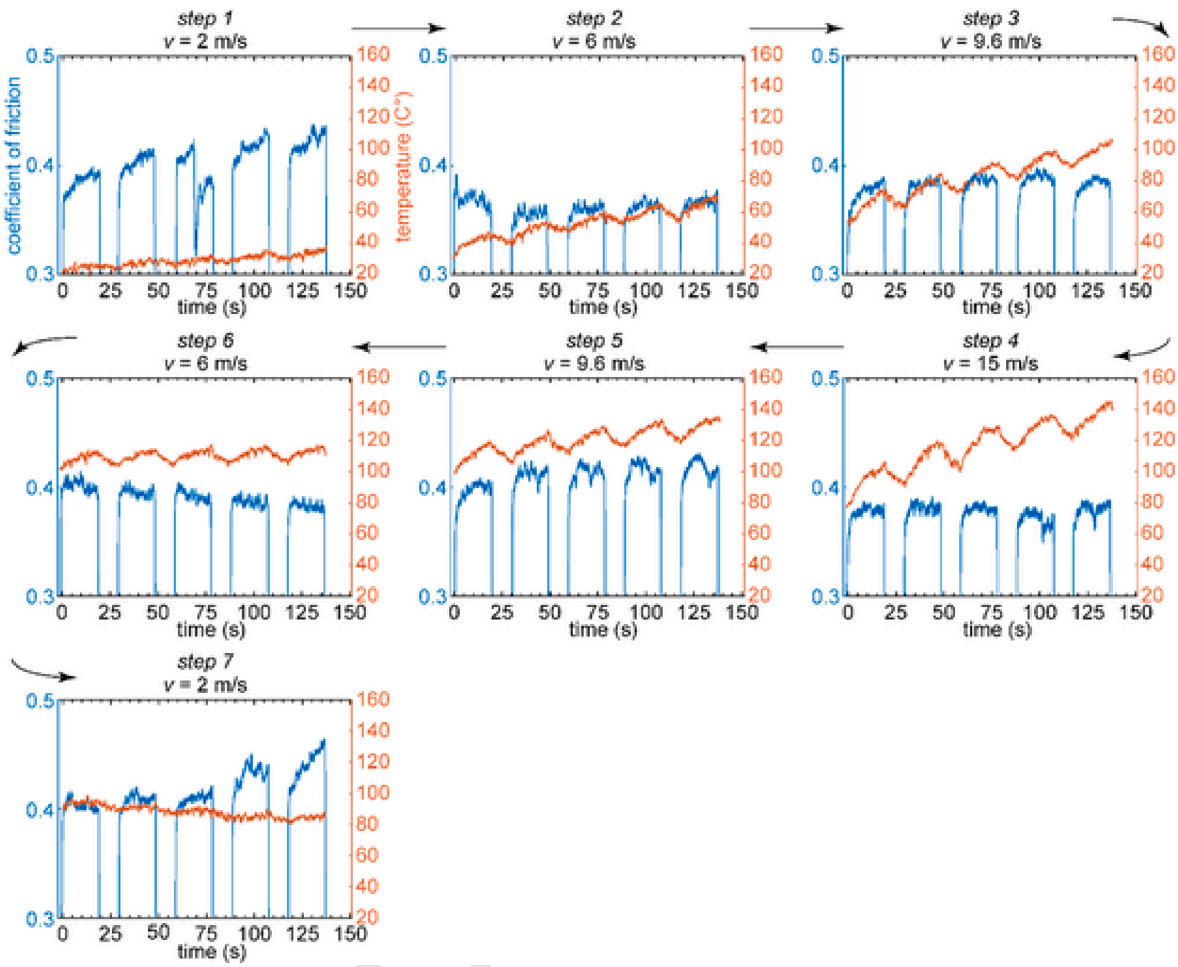

Fig. 7. In-situ monitored friction and surface temperature profiles at different sliding speeds for the Al-Ce-Ni-Mn-Zr rotor against Wilwood Purple pad material. (For interpretation of the references to colour in this figure legend, the reader is referred to the Web version of this article.)

However, the COF was unaffected and remained consistent, slightly below 0.4.

5 Step 5, speed 9 m/s: decreasing the sliding speed from 15 m/s resulted in a slight increase in the COF which was a little bit above 0.4. The temperature of the rotor kept increasing with drags and reached a peak at 133 °C.
6 Step 6, speed 6 m/s: the temperature change from first to fifth drags and the ΔT were less significant, only ~10 °C. The COF remained unaffected, ~0.4.
7 Step 7, speed 2 m/s: in the final step of the test protocol, the temperature dropped from 93°, at the beginning of the first drag, to 86° at the end of fifth drag. ΔT was unchanged.

The supplementary materials contain the same detailed analysis of the in-situ COF and temperature measurements for Al-6Cu-Mn-Zr (Fig. S2), Al-9Cu-Mn-Zr (Fig. S3), and cast iron (Fig. S4). These in-situ studies of all four rotor materials are summarized in Fig. 8 which shows a relationship between the average COF and ΔT as a function of sliding

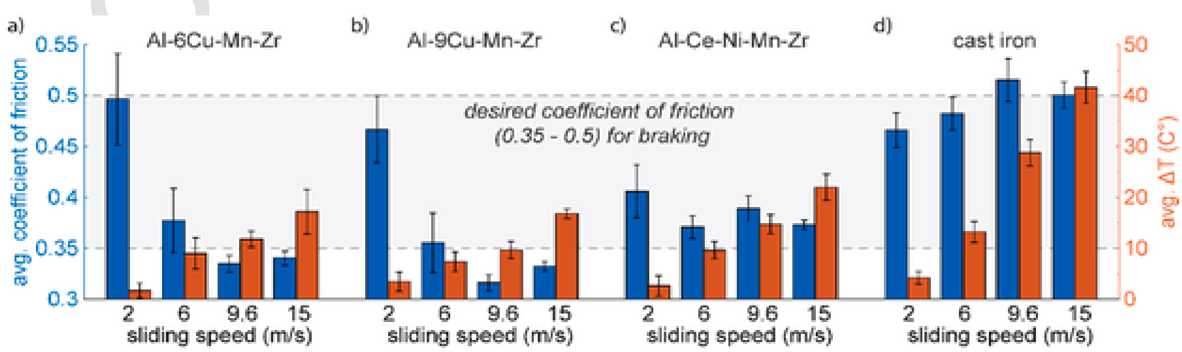

Fig. 8. Average COF and temperature increase per drag at all sliding speeds determined from the in-situ measurements for: a) Al-6Cu-Mn-Zr, b) Al-9Cu-Mn-Zr, c) Al-Ce-Ni-Mn-Zr, and d) cast iron.

speed and a range of desired COF for braking which is 0.35–0.5. Both Al-Cu-Mn-Zr alloys show very similar trends. The highest average COF was measured at the lowest sliding speed of 2 m/s (steps 1 and 7 in Fig. 8, S2, and S3). In step 1, the COF reached ~0.50 and ~0.47 for Al-6Cu-Mn-Zr and Al-9Cu-Mn-Zr, respectively. In both alloys, the COF decreased with increasing sliding speed and dropped below 0.35 at the sliding speeds of 9.6 and 15 m/s (steps, 3, 4, 5 and 6). In step 7, the COF recovers to ~0.5 as observed in step 1 for the same 2 m/s sliding speed. The measured temperatures showed similar trends as observed with Al-Ce-Ni-Mn-Zr rotor, however, the peak temperature of the Al-9Cu-Mn-Zr reached ~120 °C while the peak temperatures of Al-6Cu-Mn-Zr and Al-Ce-Ni-Mn-Zr rotors were higher, ~144 and ~143 °C, respectively.

Very different behavior of the COF was observed with the cast iron rotor, Fig. 8 and Fig. S4. The COF, peak temperature and ΔT at individual sliding speeds were much higher than the Al alloys, except the COF at 2 m/s which was comparable to Al-9Cu-Mn-Zr. The lowest COF was measured in step 1 at 2 m/s, which was slightly below 0.4. The COF then kept increasing with increasing sliding speed and temperature in steps 2, 3 and 4. At the highest sliding speed of 15 m/s in step 4, the COF reached ~0.48 which is near the upper limit of the desired COF range, and the peak temperature was 205 °C. In step 5, the speed decreased to 9.6 m/s, however, the COF increased to ~0.55 and the peak temperature reached as high as 212 °C although the ΔT was lower. As the sliding speed decreased in steps 6 and 7 the peak temperature decreased while the COF stayed constant.

The highest frictional heating parameter Φ was determined for cast iron rotor, ~1.5 × 10^{-3} (°C/J). Al alloy rotors had considerably lower values of Φ, Table 3. The lowest Φ was calculated for Al-Cu-Mn-Zr rotors, Φ ~1.0 × 10^{-3} (°C/J) while Al-Ce-Ni-Mn-Zr had Φ of ~1.2 × 10^{-3} (°C/J).

4.3. Wear performance

The worn surface morphology of each rotor material after completion of 10 km of sliding is shown in Fig. 9. All three Al alloy rotors show clear signs of abrasive wear with grooves along with the direction of sliding. Abrasive wear is less noticeable on the sliding surface of the cast iron rotor. This observation is supported by the worn surface profiles of the rotors. After 5 and 10 km of sliding, the surface of the Al alloy rotors has a very high roughness with deep grooves, while the worn surface of the cast iron rotor is much smoother, Fig. 10. The measured R_a of the worn regions was higher for the Al-Cu-Mn-Zr rotors, R_a ~2.86 and ~2.46 μm for 6Cu and 9Cu, respectively, than for the Al-Ce-Ni-Mn-Zr rotor, R_a ~1.75 μm. The roughness of the cast iron sliding surface was R_a ~0.22 μm which is only a slight increase from the unworn surface with R_a ~0.17 μm.

Abrasive wear was also observed on the worn surfaces of the pad material tested with Al alloy rotors, Fig. 11a–c. Scratches are aligned with the direction of sliding similarly to those on the worn surfaces of the Al-alloys in Fig. 9. Brake pads tested with Al-Cu-Mn-Zr alloys appear to have more pronounced abrasive wear than the pad tested with Al-Ce-Ni-Mn-Zr alloy. On the other hand, the worn surface of the pad material tested with cast iron showed only minor signs of abrasion, Fig. 11d.

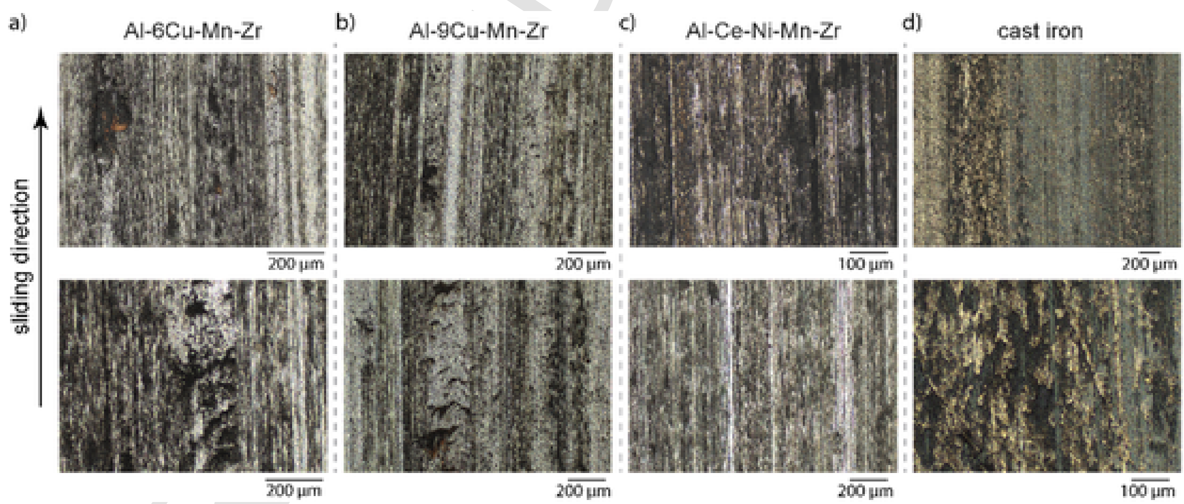

Fig. 9. Optical images of the worn sliding surfaces after 10 km of sliding. a) Al-6Cu-Mn-Zr, b) Al-9Cu-Mn-Zr, c) Al-Ce-Ni-Mn-Zr, and d) cast iron.

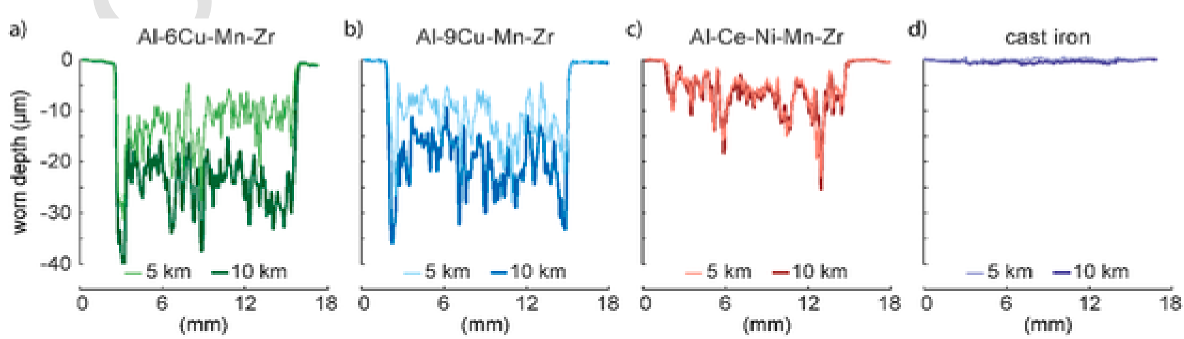

Fig. 10. Average worn rotor surface profiles of selected sections of sliding surfaces after 10 km of sliding. a) Al-6Cu-Mn-Zr, b) Al-9Cu-Mn-Zr, c) Al-Ce-Ni-Mn-Zr, and d) cast iron.

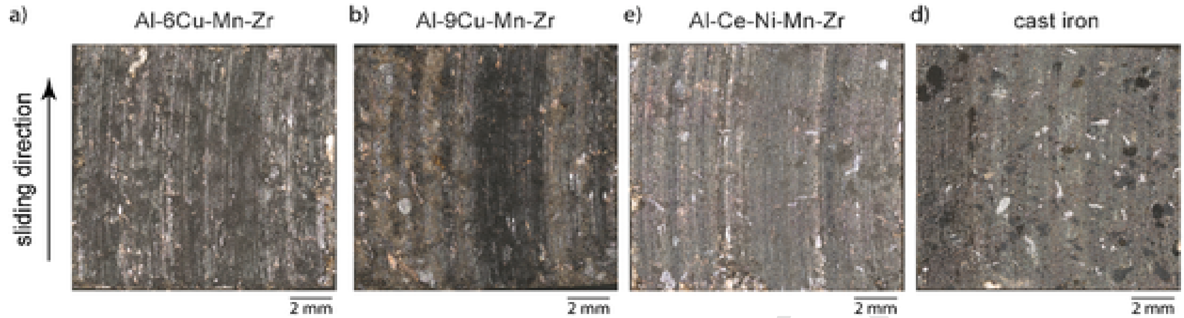

Fig. 11. Optical images of the worn sliding surfaces of the pad material after 10 km of sliding against a) Al-6Cu-Mn-Zr, b) Al-9Cu-Mn-Zr, c) Al-Ce-Ni-Mn-Zr, and d) cast iron.

The mass losses of the rotors after 5 km and 10 km of sliding showed significant differences in the wear performance of the Al-Ce-Ni-Mn-Zr and Al-Cu-Mn-Zr alloy rotors, Fig. 12a. The Al-Ce-Ni-Mn-Zr rotor had notably lower wear than the Al-Cu-Mn-Zr alloys. The mass loss of the Al-6Cu-Mn-Zr alloy after 5 km of sliding was 0.169 g and increased by ~2 times to a total of 0.320 g after additional 5 km of sliding. The mass loss of the Al-9Cu-Mn-Zr alloy after a total of 10 km of sliding was 0.255 g which is 1.8 times higher than the mass loss after 5 km of sliding, 0.142 g. The increase in the mass loss of the Al-Ce-Ni-Mn-Zr alloy rotor was the lowest, from 0.093 to 0.110 g which is only 1.2 times. Moreover, its total mass loss after 10 km of sliding is 2.9 and 2.3 times lower than that of the Al-6Cu-Mn-Zr and Al-9Cu-Mn-Zr alloys, respectively. The cast iron rotor had no measurable wear after 5 km of sliding and had a low mass loss of ~0.013 g after the additional 5 km of sliding. The wear rates normalized by load and sliding distance of the Al alloys are shown in the Supplementary Fig. S1.

The wear performance of the pad material had similar trends as those of the corresponding Al alloys, Fig. 12b. The mass losses of the pad material tested with Al-Cu-Mn-Zr alloys after 5 and 10 km of sliding rotors were similar and notably the highest. In both alloys, the mass loss of the pad was almost 0.5 g after 5 km of sliding and increased to above 0.8 g after the additional 5 km of sliding. The mass loss of the pad tested against the Al-Ce-Ni-Mn-Zr rotor after 5 km of sliding was 0.21 g which is 50 % lower than that against the Al-6Cu-Mn-Zr alloys. The mass loss increased only by 20 % after the additional 5 km of sliding. The mass loss of the pad when tested against the cast iron rotor was the lowest, 0.03 and 0.05 g after 5 and 10 km of sliding, respectively.

5. Discussion

5.1. *Frictional behavior and frictional heating*

Rapid decrease in friction from 2 m/s to higher sliding speeds in both Al-Cu-Mn-Zr alloys as illustrated in Fig. 8, could be due to a combination of insufficient pad material replenishment and surface oxidation. The purpose of the material transfer from the brake pad to the rotor is to maintain the friction coefficient around the middle of the required range of 0.35–0.5. It is hypothesized that at a relatively low speed of 2 m/s, sufficient wear debris from the pad remains at the contact interface to form a stable transfer film leading to a sliding pair of similar materials (pad-on-pad). However, at higher sliding speeds, most wear debris fall off the sliding interface due to increased vibration and a rougher surface which prevents the formation of a stable transfer film. At this stage, the rotor—pad sliding interface (a pair of dissimilar materials) likely results in a lower friction coefficient. This hypothesis can be supported by the friction behavior observed in Step 1 and Step 2 in all three aluminum alloy rotors. In step 1 during the first 20 s testing period (first drag), the friction is lower due to the initial pad – rotor sliding interface. However, as the number of drags increases, wear debris from the brake pad accumulates on the rotor's sliding surface, resulting in an increased friction. In Step 2 at 6 m/s sliding speed, friction drops after the first drag because the wear debris from the pad cannot remain on the rotor's sliding surface due to a higher vibration. The friction remains consistently low until Step 7 where the sliding speed is reduced to 2 m/s. At this slower sliding speed, wear debris from the pad can

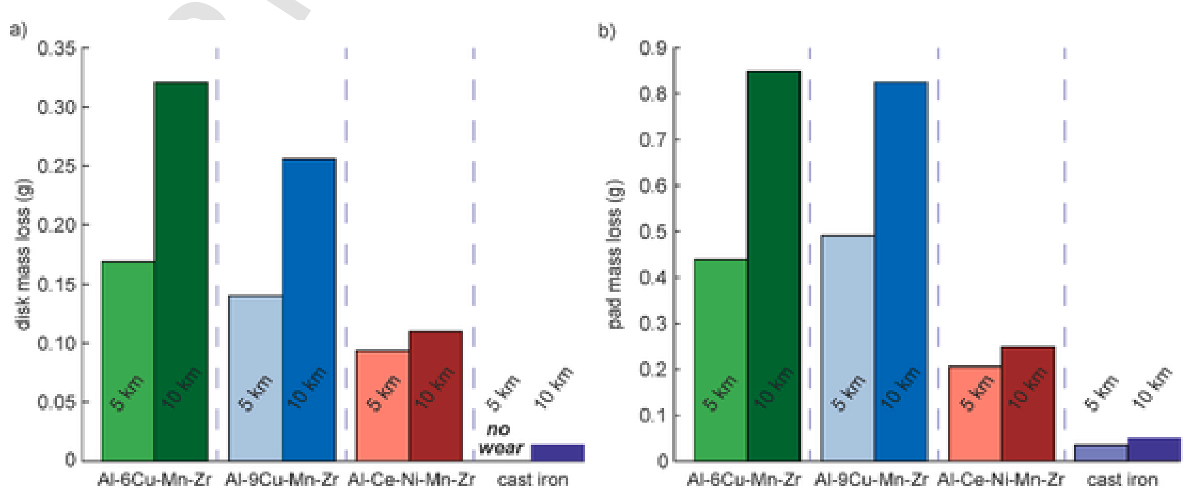

Fig. 12. Wear performance represented in mass loss after 5 and 10 km of sliding. a) The rotors of three Al alloys compared with cast iron and b) The corresponding pads.

once again accumulate on the sliding surface of the rotor causing the friction to recover to a similarly high level observed in Step 1. On the other hand, in the cast iron rotor, friction increases with the sliding speed which can be explain by a gradual formation of the transfer film. Surface oxides generated at higher sliding speeds and temperatures may also explain the decrease in friction in the tested aluminum alloys. Although the large size of the rotors prevented more detailed surface chemistry analysis using techniques such as X-ray diffraction (XRD), the composition of the brake pad suggests that the surface oxide could be carbon-rich oxides and a mix of metal oxides. One could argue that the decrease in friction performance could also be associated with low fade resistance, which is typically observed at higher surface temperatures. However, in both Al-Cu-Mn-Zr alloys the COF already rapidly decreased at 6 m/s, at which the maximum surface temperature did not exceed 70 °C, which implies that the decrease in the braking performance is not associated with a low fade resistance.

The differences in the friction behavior are more pronounced in both Al-Cu-Mn-Zr alloys than in Al-Ce-Ni-Mn-Zr alloy which shows more consistent COF over the entire range of sliding speeds. The improvement in the frictional stability in Al-Ce-Ni-Mn-Zr alloy could be due to higher oxidation resistance or, as mentioned above, due to better coverage of a transfer film on the sliding surface. To better understand the rotor/pad system resistance to fade, we examined the relationship between the COF and the rotor temperature at the highest 15 m/s sliding speed for five consecutive drags which is shown in Fig. 13. In all three Al alloy materials, the temperature increased with increasing drags, however, the COF remains consistent which suggests an excellent resistance to fade. This behavior was also observed in the reference cast iron. It can be concluded that despite the mutual wear of the Al-Ce-Ni-Mn-Zr rotor and the pad, the frictional performance is in a desired range at all sliding speeds and the braking effectiveness does not decrease at elevated temperatures.

Frictional heating parameter (Φ) described how effectively the material dissipates the energy during sliding. As expected, the calculated Φ values and measured peak temperatures show a correlation with the thermal conductivity, Table 3. Although both Al-Cu-Mn-Zr have the similar thermal conductivity and Φ values, the Al-6Cu-Mn-Zr had notably higher peak temperature. This could be explained by a higher COF at all sliding speeds.

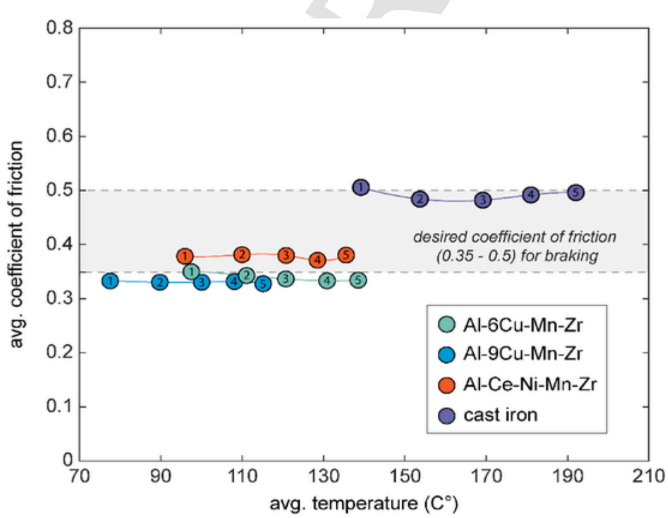

Fig. 13. Comparison of the average COF and temperature per drag for five consecutive drags at 15 m/s sliding speed for the three Al alloy rotors in comparison with the cast iron rotor.

5.2. *Wear performance*

All Al alloys showed lower wear-resistance than cast iron. Compared with Al-Cu-Mn-Zr alloys, Al-Ce-Ni-Mn-Zr shows a notable improvement in wear-resistance, especially after testing on the pre-worn rotor surface. The improved wear-resistance of Al-Ce-Ni-Mn-Zr alloy could be due to several factors, including mechanical properties, alloy composition, manufacturing process, or compatibility with the pad material. It is hypothesized that the superior wear resistance and braking performance of the Al-Ce-Ni-Mn-Zr alloy are related to its improved mechanical properties. The hardness measurements showed that the Al-Ce-Ni-Mn-Zr alloy, which is 1.6 times harder the Al-6Cu-Mn-Zr alloy, exhibited approximately 1.8 times less mass loss after 5 km of sliding. In addition to the improved hardness, previous characterization of these alloys showed that the AM Al-Ce-Ni-Mn-Zr have higher creep resistance and yield strength at 300 °C than cast Al-Cu-Mn-Zr alloys [28,33]. Moreover, the reported yield strength at 300 °C of AM Al-Ce-Ni-Mn-Zr is 176 MPa [33] while the yield strength of cast Al-Cu-Mn-Zr at 300 °C is 105 MPa [31]. Brake testing conducted in this work demonstrated that the surface temperature of these alloys can reach up to 150 °C. The improved high temperature yield strength and creep resistance of the Al-Ce-Ni-Mn-Zr alloy could be responsible for maintaining a lower wear rate and a stable COF during the brake testing. It is hypothesized that addition of Ce and Ni as alloying elements enabled preservation of hardness and strength of the AM Al-alloy rotor at high temperatures during brake testing and essentially positively impacted its wear and friction properties. Previous studies demonstrated that, in additive manufacturing processes, the improved mechanical properties of Al-Ce-Ni-Mn-Zr alloy are enabled by rapid solidification [26,28,33]. The Ce-rich and Ni-rich intermetallic phases formed at high solidification rates improve the coarsening resistance and creep and tensile properties at elevated temperatures [33].

In Al-Cu-Mn-Zr alloys, Cu did not provide the same benefits at Ce and Ni in the Al-Ce-Ni-Mn-Zr alloy. Previously, Cu had been shown to improve castability, but not creep resistance [31]. Hardness testing conducted in this work suggested that a higher concentration of Cu increased the hardness. The improvement in the wear resistance of the Al-9Cu-Mn-Zr compared with the Al-6Cu-Mn-Zr alloy could be correlated to the improvement in the hardness. Additionally, Cu additives are used in tribological applications to reduce friction and wear [44] [45] which could have also contributed to the lower mass loss of the Al-9Cu-Mn-Zr rotor. Nevertheless, Cu-based Al-alloys tested in this work do not seem to be ideal for brake applications.

Al-Ce-Ni-Mn-Zr showed a significant improvement in wear-resistance after the second round of testing. It is hypothesized that this improvement is facilitated by formation of a stable transfer film after the first round of testing, which could be due to several factors. The higher hardness and yield strength of Al-Ce-Ni-Mn-Zr could decrease the initial wear and reduce the surface roughness, which could be beneficial in forming the transfer film from the pad material. Additionally, the composition of Al-Ce-Ni-Mn-Zr alloy could be more compatible with the composition of the brake pad, which could have contributed to the formation of a more stable transfer film. However, the optical images revealed the formation of a patchy discontinuous transfer film on all three Al alloys and cast iron, which was deduced from the observation of darker patch-like regions on the sliding surface, Fig. 9. To validate this claim, we performed SEM-EDS analysis of the sliding surface of Al-Ce-Ni-Mn-Zr after 10 km of sliding. The elemental mapping revealed discontinuous "patchy" regions composed of elements such as Ba, Ca, S, Si, and Cu, Fig. 14. These elements were also identified in the pad material, Fig. 2., which suggests the pad material transferred to the surface of the rotor during sliding. SEM-EDS analysis of the sliding surface of the brake pads tested with Al-Ce-Ni-Mn-Zr and Al-6Cu-Mn-Zr rotors shown in the Supplementary Figs. S5 and S6, respectively, also revealed a metallic transfer on the pad surface. In both cases, elemental

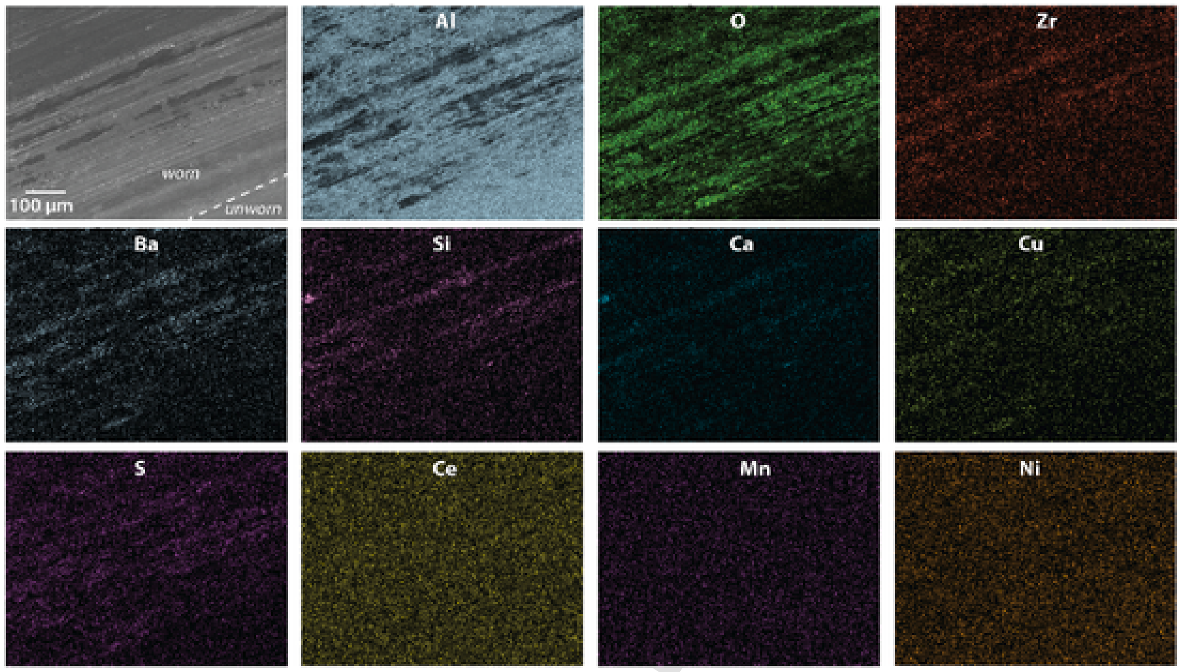

Fig. 14. SEM images and EDS elemental maps of the wear track on the Al-Ce-Ni-Mn-Zr rotor after 10 km of sliding.

maps show regions with higher concentration of Al than the unworn pad in Fig. 3. The elemental maps of the sliding surface of the pad tested with the cast iron rotor in Supplemental Fig. S7 show a uniform coverage of cast iron, however, the intensity peak is rather small which suggest that the metallic transfer was less significant than with the Al alloy rotors.

Since the transfer film was not fully formed, it is plausible that some other mechanism enabled a significant improvement in the wear-resistance of the Al-Ce-Ni-Mn-Zr rotor after the second round of testing. A comparison of the worn surface profiles in Fig. 10 showed that both Al-Cu-Mn-Zr rotors have different shapes of the worn surface profiles after 5 km vs 10 km of sliding, which indicates that a conforming contact between the rotor and the pad has not been established yet and the wear process is still in the transient run-in period. On the other hand, the worn surface profiles after 5 km vs 10 km in Al-Ce-Ni-Mn-Zr have almost identical shape and there is a very small difference in the worn depth. This observation implies that the rotor-pad interface has reached a conforming contact and the worn surface recesses at a steady-state rate which is much lower than the recession rate in the run-in regime. When the wearing surface topography reaches a steady-state condition, the wear continues at a constant lower rate than the transient run-in period, which has been demonstrated numerically in other studies [46–49].

The wear performance of the pad material is also essential for evaluating the rotor-pad compatibility. While material removal of the pad is needed to enable formation of a transfer film, excessive wear is not acceptable. Despite the relatively high wear of the Al alloy rotors, an unexpectedly high wear also occurred in the pad material. Curiously, for the rotor-pad materials studied here, the softest and least wear resistant Al-Cu-Mn-Zr rotor materials resulted in the highest wear of the pad material. This phenomenon may be difficult to interpret since the precise composition of the commercial brake pad material is unknown. One plausible explanation can be deduced from the morphology of the worn surface. The roughness of the sliding surfaces of both Al-Cu-Mn-Zr rotors is much higher than that of Al-Ce-Ni-Mn-Zr. The prominent sharp ridges, as observed in the average worn surface profiles in Fig. 10a and b, acted as stress concentrators and increased the local contact pressures during sliding which could have led to increased material removal of rotor-pad interface. This hypothesis is also supported from the analysis of the worn surfaces of the cast iron rotor-pad pair in which both sliding surfaces had only minor signs of abrasion Figs. 9d and 11d.

Formation of a fully continuous steady transfer film on the sliding surface of the high temperature Al alloy rotors studied here could have resulted in an optimal wear of the rotor-pad pair as observed in the reference cast iron. Although a steady transfer film was not formed in cast iron, the significantly lower mass loss of the rotor and the pad was attributed to the high hardness of cast iron. The results of this wear analysis imply that the pad material is not compatible for the Al alloys studied here, however, Al-Ce-Ni-Mn-Zr alloy showed a potential to be a candidate light-weight brake rotor material due to remarkably improved wear-resistance after sliding on the pre-worn surface.

A limitation of this study is that the tested aluminum alloys have varying compositions and were fabricated using different methods, yet their individual effects on braking performance were not studied separately. However, based on the results it can be deduced that the composition of Al-Ce-Ni-Mn-Zr alloy combined with the rapid solidification characteristics of the AM process contributed to the improved braking performance. The effect of composition and process parameters will be explored in future studies.

5.3. Potential of high-temperature aluminum alloys as brake rotor materials

The goal of this work was to characterize the braking performance of high temperature Al alloys and to discuss their feasibility to be used as brake rotor materials. The qualifying metrics were wear-resistance, frictional behavior, and frictional heating in comparison to traditionally used cast iron. Among all three candidate Al alloys, Al-Ce-Ni-Mn-Zr had superior wear-resistance and frictional behavior to Al-Cu-Mn-Zr but did not outperform cast iron. However, regenerative braking in EVs minimizes the use of conventional braking and lessens the demand for high wear-resistance materials, which provides opportunities for the use of Al alloys. The frequency of applying brakes in EVs depends on several circumstances, such as road conditions, traffic, and driving style of an individual, nevertheless, the regenerative braking accounts for most of the braking in EVs [17]. The wear-resistance of Al-Ce-Ni-Mn-Zr may be adequate to accommodate for the less frequent application of friction-type brakes.

One of the downsides of the Al alloys studied here is their lower COF at higher sliding speeds. Although the COF of Al-Ce-Ni-Mn-Zr stayed within a desired range for braking, the COF of cast iron was notably higher. During braking, weight and momentum are transferred to the front of the vehicle which puts more braking demands on the front rotors as they get hotter than the rear rotors. Moreover, the front brakes also need to withstand higher applied forces from the brake pad. The disadvantage of the lower COF and lower wear-resistance of Al alloy rotors could be overcome by placing them in the rear end of the EV while keeping cast iron rotor in the front.

Al alloys have a higher thermal conductivity than cast iron, which significantly improves their thermal management. Due to higher heat dissipation rates, the surface of the Al alloy rotors is cooler, which is desirable for the braking performance. However, more heat is transferred to the surrounding parts due to the high thermal conductivity of the braking components, which could present challenges.

Formation of a transfer layer on the sliding surface of the rotors is essential for achieving optimal friction and wear performance of a rotor-pad pair. The Al alloys studied in this work formed only a patchy discontinuous transfer layer which was attributed to a compatibility mismatch between the brake pad and the Al alloy materials. However, selection of a more compatible brake pad material may be difficult. The brake pad material used in this work was selected based on screening over 15 different pad materials among which several were designed for Al alloy rotors. Designing ideal brake pad material for the studied Al alloy rotors was beyond the scope of this work.

Although replacing traditionally used cast iron rotors with Al alloys presents challenges, Al materials have been successfully integrated in various parts of the brake systems. For example, Al is used in brake rotors for motorbikes which require less braking demand or as brake calipers for lightweighting and corrosion benefits. Future work will focus on optimizing properties such as hardness and thermal conductivity of these high temperature Al alloys and selecting more compatible pad materials which could lead to improved wear-resistance and braking performance.

6. Conclusions

Braking performance has been characterized on three advanced high-temperature Al alloys using a sub-scale brake tester over a range of sliding speeds to evaluate their feasibility as brake rotor materials. Wear-resistance, friction behavior, and surface temperature increase of the candidate Al alloys were compared with those of the traditionally used cast iron. The following conclusions were made based on characterization of the mechanical properties and the worn surface morphologies:

1 Additively manufactured Al-Ce-Ni-Mn-Zr showed significantly higher wear resistance than the cast Al-6Cu-Mn-Zr and Al-9Cu-Mn-Zr alloys, which was attributed to the higher hardness and better compatibility with the pad material. The wear performance of Al-Ce-Ni-Mn-Zr was notably improved when the sliding surface was pre-worn.
2 The AM Al-Ce-Ni-Mn-Zr alloy showed promising braking performance. The COF was within the desirable range of 0.35–0.50 at all sliding speeds, even at elevated surface temperatures. In contrast, the COF of the Al-Cu-Mn-Zr alloys decreased rapidly at higher sliding speeds to below the desired range.
3 Al-Ce-Ni-Mn-Zr and both Al-Cu-Mn-Zr alloys had lower peak temperatures and temperature rises per drag than cast iron, which was correlated with their higher thermal conductivities. Brake testing at the highest sliding speed of 15 m/s showed a consistent COF for five consecutive drags, which suggests a good resistance to fade.
4 Characterization of the sliding surfaces revealed that the candidate Al alloys formed a patchy discontinuous transfer film. It is hypothesized that formation of a steady fully formed transfer layer would improve the braking performance.
5 Al-Ce-Ni-Mn-Zr demonstrated a potential to be used as a brake rotor material for EVs, in which the conventional braking is utilized less frequently. Although Al-Cu-Mn-Zr rotor had an inferior wear resistance and braking performance than the conventional cast iron rotor, its lightweight, corrosion resistance, and improved fade resistance could have beneficial impact for EV vehicles.

Notice

This manuscript has been authored by UT-Battelle, LLC and Battelle Energy Alliance, LLC, under contract DE-AC05-00OR22725 with the US Department of Energy (DOE). The US Government retains and the publisher, by accepting the article for publication, acknowledges that the US government retains a nonexclusive, paid-up, irrevocable, worldwide license to publish or reproduce the published form of this manuscript, or allow others to do so, for US government purposes. DOE will provide public access to these results of federally sponsored research in accordance with the DOE Public Access Plan (http://energy.gov/downloads/doe-public-access-plan).

Confirmation of authorship

We confirm that the manuscript has been read and approved by all named authors and that there are no other persons who satisfied the criteria for authorship but are not listed. We further confirm that the order of authors listed in the manuscript has been approved by all of us.

Declaration of competing interest

The authors declare that they have no known competing financial interests or personal relationships that could have appeared to influence the work reported in this paper.

Acknowledgements

The research was sponsored by the Powertrain Materials Core Program, Vehicle Technologies Office, US Department of Energy (DOE). The authors thank Daniel Fleming and Douglas Stringfield for helping with samples preparation, Dana McClurg for conducting thermal conductivity measurements, James Burns and Jonathan Poplawsky for their assistance with the SEM and EDS analysis of the rotor.

Appendix A. Supplementary data

Supplementary data to this article can be found online at https://doi.org/10.1016/j.wear.2025.205961.

References

[1] A.J. Day, D. Bryant, Braking of Road Vehicles, second ed., Butterworth-Heinemann, Kidlington, UK; Cambridge, MA, USA, 2022 978-0-12-822005-4.
[2] S.M.S. Wahid, Automotive brake wear: a review, Environ. Sci. Pollut. Control Ser. 25 (2018) 174–180.
[3] A. Papinniemi, J.C.S. Lai, J. Zhao, L. Loader, Brake squeal: a literature review, Appl. Acoust. 63 (2002) 391–400.
[4] J. Zang, Z. Yang, M. Sun, Z. Li, Y. Wang, S. Ye, Simulation-based microstructural analysis of thermal–mechanical fatigue behavior in SiCp/A356 composites for brake disc applications, J. Mater. Sci. 59 (2024) 650–668.
[5] T. Grigoratos, G. Martini, Brake wear particle emissions: a review, Environ. Sci. Pollut. Control Ser. 22 (2015) 2491–2504.

[6] J.K. Katiyar, S. Bhattacharya, V. Kumar, P. Vikram, K, Automotive Tribology, Springer Singapore, Singapore, 2019, https://doi.org/10.1007/978-981-15-0434-1.
[7] M. Motta, L. Fedrizzi, F. Andreatta, Corrosion stiction in automotive braking systems, Materials 16 (2023) 3710.
[8] C.B.N.S. Abhishikt, B. Ramachandran, G.N. Alekhya, Design and analysis of disk rotor brake under tribological behaviour of materials, in: Materials Today: Proceedings, vol. 33, Elsevier Ltd, 2020, pp. 4298–4310.
[9] A. Rashid, Overview of disc brakes and related phenomena - a review, Int. J. Veh. Noise Vib. 10 (2014) 257.
[10] A.J. Day, M. Tirovic, T.P. Newcomb, Thermal effects and pressure distributions in brakes, Proc. Inst. Mech. Eng. - Part D J. Automob. Eng. 205 (1991) 199–205.
[11] P. Zhang, L. Zhang, K. Fu, P. Wu, J. Cao, C. Shijia, X. Qu, Fade behaviour of copper-based brake pad during cyclic emergency braking at high speed and overload condition, Wear 428–429 (2019) 10–23.
[12] Y. Hui, G. Liu, Q. Zhang, Y. Zhang, Y. Zang, S. Wang, R. Shi, Fading behavior and wear mechanisms of C/C–SiC brake disc during cyclic braking, Wear (2023) 526–527.
[13] P.J. Blau, B.C. Jolly, J. Qu, W.H. Peter, C.A. Blue, Tribological investigation of titanium-based materials for brakes, Wear 263 (2007) 1202–1211.
[14] S. Awe, A. Thomas, The prospects of lightweight SICAlight discs in the emerging disc brake requirements. EuroBrake 2021 Technical Programme, 2021.
[15] J.A. Sanguesa, V. Torres-Sanz, P. Garrido, F.J. Martinez, J.M. Marquez-Barja, A review on electric vehicles: Technologies and challenges, Smart Cities 4 (2021) 372–404.
[16] C. Yang, T. Sun, W. Wang, Y. Li, Y. Zhang, M. Zha, Regenerative braking system development and perspectives for electric vehicles: an overview, Renew. Sustain. Energy Rev. 198 (2024) 114389.
[17] S. Awe, Sustainable aluminium brake discs and pads for electrified vehicles, in: Proceedings Of the FISITA - Technology and Mobility Conference Europe 2023 Barcelona, Spain: FISITA, 2023, https://doi.org/10.46720/eb2023-tst-020.
[18] S.A. Awe, Developing material requirements for automotive brake disc, Mod. Concep. Mater. Sci. 2 (2019).
[19] A. Rashid, Overview of disc brakes and related phenomena - a review, Int. J. Veh. Noise Vib. 10 (2014) 257.
[20] National Research Council, Cost, Effectiveness, and Deployment of Fuel Economy Technologies for Light-Duty Vehicles, National Academies Press, Washington, D.C., 2015. http://www.nap.edu/catalog/21744.
[21] Y. Lyu, J. Wahlström, M. Tu, U. Olofsson, A friction, wear and emission Tribometer study of non-asbestos organic pins sliding against AlSiC MMC discs, Tribol. Ind. 40 (2018) 274–282.
[22] A. Du, L. Lattanzi, A.E.W. Jarfors, J. Zheng, K. Wang, G. Yu, Role of matrix alloy, reinforcement size and fraction in the sliding wear behaviour of Al-SiCp MMCs against brake pad material, Wear (2023) 530–531.
[23] F. Gulden, B. Reinhold, S. Gramstat, A. Stich, U. Tetzlaff, H.W. Höppel, "Investigation of the run-in and corrosion behavior of a PEO-coated aluminum brake disc", in: P.E. Pfeffer (Ed.), Proceedings, 10th International Munich Chassis Symposium 2019, Springer Vieweg, Wiesbaden, 2020, pp. 611–631.
[24] P.J. Blau, "Prospects for Titanium-Based Materials as Truck Disc Brake Rotors" (ORNL Tech Report, ORNL TM-2007-111, 2007.
[25] J. Qu, P.J. Blau, B.C. Jolly, Oxygen-diffused titanium as a candidate brake rotor material, Wear 267 (2009) 818–822.
[26] R.A. Michi, A. Plotkowski, A. Shyam, R.R. Dehoff, S.S. Babu, Towards high-temperature applications of aluminium alloys enabled by additive manufacturing, Int. Mater. Rev. 67 (2022) 298–345.
[27] S. Bahl, L. Xiong, L.F. Allard, R.A. Michi, J.D. Poplawsky, A.C. Chuang, D. Singh, T.R. Watkins, D. Shin, J.A. Haynes, A. Shyam, Aging behavior and strengthening mechanisms of coarsening resistant metastable θ' precipitates in an Al–Cu alloy, Mater. Des. 198 (2021) 109378.
[28] R.A. Michi, K. Sisco, S. Bahl, Y. Yang, J.D. Poplawsky, L.F. Allard, R.R. Dehoff, A. Plotkowski, A. Shyam, A creep-resistant additively manufactured Al-Ce-Ni-Mn alloy, Acta Mater. 227 (2022) 117699.
[29] R.A. Michi, K. Sisco, S. Bahl, Y. Yang, J.D. Poplawsky, L.F. Allard, R.R. Dehoff, A. Plotkowski, A. Shyam, A creep-resistant additively manufactured Al-Ce-Ni-Mn alloy, Acta Mater. 227 (2022).
[30] J.D. Poplawsky, B.K. Milligan, L.F. Allard, D. Shin, P. Shower, M.F. Chisholm, A. Shyam, The synergistic role of Mn and Zr/Ti in producing θ′/L12 co-precipitates in Al-Cu alloys, Acta Mater. 194 (2020) 577–586.
[31] A. Shyam, S. Roy, D. Shin, J.D. Poplawsky, L.F. Allard, Y. Yamamoto, J.R. Morris, B. Mazumder, J.C. Idrobo, A. Rodriguez, T.R. Watkins, J.A. Haynes, Elevated temperature microstructural stability in cast AlCuMnZr alloys through solute segregation, Mater. Sci. Eng. 765 (2019) 138279.
[32] J.U. Rakhmonov, S. Bahl, A. Shyam, D.C. Dunand, Cavitation-resistant intergranular precipitates enhance creep performance of θ′-strengthened Al-Cu based alloys, Acta Mater. 228 (2022) 117788.
[33] S. Bahl, T. Wu, R.A. Michi, K. An, D. Yu, L.F. Allard, J.U. Rakhmonov, J.D. Poplawsky, C.M. Fancher, D.C. Dunand, A. Plotkowski, A. Shyam, An additively manufactured near-eutectic Al-Ce-Ni-Mn-Zr alloy with high creep resistance, Acta Mater. 268 (2024) 119787.
[34] M. Javidani, D. Larouche, Application of cast Al–Si alloys in internal combustion engine components, Int. Mater. Rev. 59 (2014) 132–158.
[35] S. Roy, L.F. Allard, A. Rodriguez, W.D. Porter, A. Shyam, Comparative evaluation of cast aluminum alloys for automotive cylinder heads: Part II—mechanical and thermal properties, Metall. Mater. Trans. 48 (2017) 2543–2562.
[36] S. Roy, L.F. Allard, A. Rodriguez, T.R. Watkins, A. Shyam, Comparative evaluation of cast aluminum alloys for automotive cylinder heads: Part I—microstructure evolution, Metall. Mater. Trans. 48 (2017) 2529–2542.
[37] J. Ding, C. Cui, Y. Sun, L. Zhao, S. Cui, Effect of Mo, Zr, and Y on the high-temperature properties of Al–Cu–Mn alloy, J. Mater. Res. 34 (2019) 3853–3861.
[38] S. Griffiths, J.R. Croteau, M.D. Rossell, R. Erni, A. De Luca, N.Q. Vo, D.C. Dunand, C. Leinenbach, Coarsening- and creep resistance of precipitation-strengthened Al–Mg–Zr alloys processed by selective laser melting, Acta Mater. 188 (2020) 192–202.
[39] J. Deng, C. Chen, X. Liu, Y. Li, K. Zhou, S. Guo, A high-strength heat-resistant Al–5.7Ni eutectic alloy with spherical Al3Ni nano-particles by selective laser melting, Scr. Mater. 203 (2021) 114034.
[40] L. Zhou, T. Huynh, S. Park, H. Hyer, A. Mehta, S. Song, Y. Bai, B. McWilliams, K. Cho, Y. Sohn, Laser powder bed fusion of Al–10 wt% Ce alloys: microstructure and tensile property, J. Mater. Sci. 55 (2020) 14611–14625.
[41] D.M. Stefanescu, Physical properties of cast irons, in: Cast Iron Science and Technology, ASM International, 2017, pp. 413–429.
[42] G. Wang, Y. Li, Thermal conductivity of cast iron -A review, China Foundry 17 (2020) 85–95.
[43] R.L. Hecht, R.B. Dinwiddie, W.D. Porter, H. Wang, Thermal transport properties of grey cast irons, SAE Techn. Pap. 10 (1996) 1699–1705.
[44] F.L. Guzman Borda, S.J. Ribeiro de Oliveira, L.M. Seabra Monteiro Lazaro, A.J. Kalab Leiróz, Experimental investigation of the tribological behavior of lubricants with additive containing copper nanoparticles, Tribol. Int. 117 (2018) 52–58.
[45] J. Padgurskas, R. Rukuiza, I. Prosyčevas, R. Kreivaitis, Tribological properties of lubricant additives of Fe, Cu and Co nanoparticles, Tribol. Int. 60 (2013) 224–232.
[46] X. Jia, T. Grejtak, B. Krick, N. Vermaak, Topology optimization of tribological composites for multifunctional performance at sliding interfaces, Compos. B Eng. 199 (2020) 108209.
[47] T. Grejtak, X. Jia, F. Feppon, S.G. Joynson, A.R. Cunniffe, Y. Shi, D.P. Kauffman, N. Vermaak, B.A. Krick, Topology optimization of composite materials for wear: a route to multifunctional materials for sliding interfaces, Adv. Eng. Mater. 21 (2019) 1–13.
[48] X. Jia, T. Grejtak, B. Krick, N. Vermaak, Experimentally calibrated abrasive sliding wear Model: demonstrations for rotary and linear wear systems, J. Appl. Mech. 85 (2018) 121011.
[49] X. Jia, T. Grejtak, B. Krick, N. Vermaak, Design of composite systems for rotary wear applications, Mater. Des. 134 (2017) 281–292.